

Observation of the Emergence of Multipartite Entanglement Between a Bipartite System and its Environment

O. Jiménez Farías, G. H. Aguilar, A. Valdés-Hernández, P. H. Souto Ribeiro, L. Davidovich, and S. P. Walborn
Instituto de Física, Universidade Federal do Rio de Janeiro, Caixa Postal 68528, Rio de Janeiro, RJ 21941-972, Brazil

(Received 8 June 2012; published 9 October 2012)

The dynamics of the environment is usually experimentally inaccessible and hence ignored for open systems. Here we overcome this limitation by using an interferometric setup that allows the implementation of several decoherence channels and full access to all environmental degrees of freedom. We show that when a qubit from an entangled pair interacts with the environment, the initial bipartite entanglement gets redistributed into bipartite and genuine multipartite entanglements involving the two qubits and the environment. This is yet another trait of the subtle behavior of entangled open systems.

DOI: [10.1103/PhysRevLett.109.150403](https://doi.org/10.1103/PhysRevLett.109.150403)

PACS numbers: 03.65.Yz, 03.67.Bg, 03.67.Mn, 42.50.Dv

The fragility of quantum coherence and entanglement following interaction with the environment is one of the main obstacles to the realization of quantum information tasks such as quantum computation, quantum communication, and precision measurements. It also plays an important role in the study of the classical limit of quantum mechanics. Indeed, the emergence of the classical world from the quantum substrate is intimately connected to the interaction between quantum systems and their environments [1–3], which accounts for the irreversible information flow out of an open system. The corresponding dynamical description frequently ignores the evolution of the environment itself, which is considered beyond any realistic attempt of experimental analysis. Yet, the consideration of this dynamics may help us to increase the robustness of the quantum information processes and also clarify the subtle characteristics of quantum-classical transition, like the emergence of pointer states [2,3] and the eventual disappearance of entanglement in open systems that still exhibit coherence between their parts [4–8]. Pointer states remain unchanged under interaction with the environment, which, as shown in Refs. [9,10], stores multiple copies of these states, so that a tiny fraction of the environment may be sufficient to reveal the state of the system. This is an essential trait of the classical world, which can thus be uncovered by the detailed study of the dynamical structure of the environment: in order to recognize a classical object, one does not need to probe its whole surroundings. This motivates some corresponding questions with regard to entanglement. As it decays and eventually disappears, what is its imprint on the environment? A theoretical analysis of the redistribution of entanglement between a system and its surroundings was initiated in Refs. [7,8]. However, the experimental observation of this phenomenon is quite challenging, since the environment is usually inaccessible to measurement.

We overcome this difficulty by means of an experimental setup that allows full access to the environmental degrees of freedom. We use this device to investigate the

dynamics of entanglement when one qubit of an entangled pair interacts with an environment, and generalize the work in Ref. [11], which demonstrated theoretically and experimentally that for the amplitude decay (AD) channel, there are bipartite entanglement invariants involving the two qubits and the environment. We implement with our interferometric device two paradigmatic models of decoherence, corresponding to AD and phase damping (PD). We analyze the two-qubit system and its environment using the complete quantum state tomography, including measurement of the coherences of the environment. Therefore, we were able to monitor the emergence and evolution of the genuine multipartite entanglement between the system qubits and the environment qubit. Two inequivalent families of genuinely entangled states [12] may arise, depending on the decoherence mechanism and the initial state: Greenberger-Horne-Zeilinger (GHZ) states [13] of the form $(|000\rangle + |111\rangle)/\sqrt{2}$, and W states [12], defined as $(|100\rangle + |010\rangle + |001\rangle)/\sqrt{3}$. We characterize the genuine multipartite entanglement by using lower bounds (LBs) and approximations for the entanglement measures, as well as entanglement witnesses, which are quite useful within the present framework.

We developed the experimental setup shown in Fig. 1, which allows for the complete control and measurement of the environment degrees of freedom in an all-optical setup. Pairs of polarization-entangled photons are produced using spontaneous parametric down-conversion [14]. Photon A goes directly to polarization analysis, while the polarization of photon B is subject to an interaction with the environment, E , encoded in two spatial modes. A complete quantum state tomography is performed on the three systems (bipartite system + environment) using a combination of two highly stable nested interferometers.

The first block, shown in Fig. 1(b), is used to implement the decoherence channels in similarity to what was done in Refs. [15,16]. A qubit encoded in the polarization of a single photon (system B) passes through a birefringent calcite beam displacer (BD), which deviates the horizontal

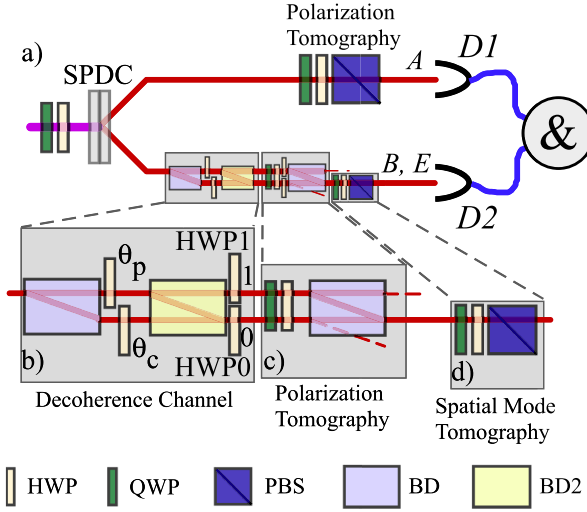


FIG. 1 (color online). Experimental setup. Two polarization-entangled photons ($\lambda = 650$ nm) are produced by a two-crystal spontaneous parametric down converter SPDC [14] pumped by a cw He-Cd laser ($\lambda = 325$ nm). One photon is sent straight to a standard polarization analysis consisting of a quarter-wave plate (QWP), a half-wave plate (HWP), a polarizing beam splitter (PBS), and a single-photon detector equipped, with a 10 nm FWHM interference filter. The other photon is sent through two nested interferometers. The first one implements the decoherence channels described by Eqs. (1) and (2), while the second interferometer performs projections for the quantum state tomography on both systems B and E (see text).

(H) component and transmits the vertical (V) one. At the output of this BD, the H and V components are spatially separated so that each one can be rotated independently with the wave plates HWP(θ_c) and HWP(θ_p). The first plate is fixed at $\theta_c = 0$ and ensures that the two optical path lengths are identical, while the angle θ_p in the second plate varies as $0 \leq \theta_p \leq \pi/4$. The second beam displacer (BD2) deviates the V polarization and transmits the H polarization [17]. If no rotation is induced in the V component ($\theta_p = 0$), the modes H and V are coherently recombined completely in the spatial mode we call mode 0. As θ_p varies, the spatial mode 1 populates according to

$$|0\rangle_B|0\rangle_E \rightarrow |0\rangle_B|0\rangle_E, \quad (1a)$$

$$|1\rangle_B|0\rangle_E \rightarrow \sqrt{1-p}|1\rangle_B|0\rangle_E + \sqrt{p}|0\rangle_B|1\rangle_E, \quad (1b)$$

where H (V) represents the 0 (1) state in the computational basis and $p = \sin^2\theta_p$. This map corresponds to the AD channel [18], where $p = p(t)$ is a time parametrization (recovered here for different angles θ_p) such that $p(0) = 0$, $p(\infty) = 1$.

However, if we rotate the polarization in the spatial mode 1 using a HWP1 at $\pi/4$, the resulting channel can be described by

$$|0\rangle_B|0\rangle_E \rightarrow |0\rangle_B|0\rangle_E, \quad (2a)$$

$$|1\rangle_B|0\rangle_E \rightarrow \sqrt{1-p}|1\rangle_B|0\rangle_E + \sqrt{p}|1\rangle_B|1\rangle_E, \quad (2b)$$

since HWP1 transforms the state $|0\rangle_B$ (H polarization) into the state $|1\rangle_B$ (V polarization). HWP0 equates the optical path lengths. This map represents the PD channel [18].

The second block shown in Fig. 1(c) has two purposes: (i) to perform tomographic measurements on the polarization, and (ii) to coherently recombine modes 0 and 1. Polarization analysis of system B is carried out using a QWP, a HWP, and the third BD. For polarization tomography, this BD plays the role of a polarizer. From the spatial walk-off in the BD, an H -polarized mode at the output corresponds to propagation mode 1 and a V -polarized mode to propagation mode 0. Since this BD also allows for coherent recombination of modes 0 and 1, the superpositions of these modes are mapped into the superpositions of H and V polarizations at the output of the BD. Thus, information of the spatial modes before the BD is mapped into the polarization modes, and is finally analyzed in the spatial mode tomography block, shown in Fig. 1(d). In this way, the projective measurements of each subsystem correspond to the setting up of a QWP and HWP. Therefore, the configuration of the three pairs of wave plates (two for each subsystem) and the coincidence detection in $D1$ and $D2$, also shown in Fig. 1, represent the projective measurements of the global tripartite system. In this case, 64 measurements were needed to perform the full quantum state tomography. When compared to previous studies [5,11,19], the configuration shown in Fig. 1 has the advantage of allowing for the complete tomographic measurement of the environment in a stable fashion.

With the three systems A , B , and E , we could explore the dynamics of entanglement as a function of p for the PD and AD channels. To illustrate the emergence of a multipartite entanglement and motivate the discussion that follows, we first consider the case of pure states. For the PD channel, we consider the initial state, corresponding to $p = 0$:

$$|\varphi(0)\rangle_{ABE} = \frac{1}{\sqrt{2}}[|11\rangle_{AB} + |00\rangle_{AB}]|0\rangle_E. \quad (3)$$

The PD interaction produces a tripartite state,

$$|\varphi(p)\rangle_{ABE} = \frac{1}{\sqrt{2}}[|000\rangle + \sqrt{1-p}|110\rangle + \sqrt{p}|111\rangle], \quad (4)$$

which for $p = 1$ becomes a GHZ state.

For the AD channel Eq. (1), let us consider the initial state

$$|\eta(0)\rangle_{ABE} = \left[\sqrt{\frac{1}{3}}|10\rangle + \sqrt{\frac{2}{3}}|01\rangle \right]_{AB} |0\rangle_E, \quad (5)$$

which evolves to

$$|\eta(p)\rangle_{ABE} = \sqrt{\frac{1}{3}}|100\rangle + \sqrt{\frac{2}{3}}[\sqrt{1-p}|010\rangle + \sqrt{p}|001\rangle]. \quad (6)$$

The states in Eqs. (4) and (6) can present (i) bipartite entanglement between systems A and B , and between each of them and the environment E , (ii) bipartite entanglement between each system and the remaining two (taken as a single system), and (iii) genuine tripartite entanglement, as in the GHZ and W states mentioned above. The bipartite entanglements can be quantified using the concurrence C [20] or, equivalently, the tangle $\mathcal{T} = C^2$. The entanglement between the pairs of qubits i and j in states of the form $\rho_{ij} = \text{Tr}_k(\rho)$ can be calculated using the definition $\mathcal{T}_{ij} = [\max\{0, \Lambda\}]^2$, where $\Lambda = \sqrt{\lambda_1} - \sqrt{\lambda_2} - \sqrt{\lambda_3} - \sqrt{\lambda_4}$ and λ_m are the positive eigenvalues of the matrix $\rho_{ij}(\sigma_y \otimes \sigma_y)\rho_{ij}^*(\sigma_y \otimes \sigma_y)$ in decreasing order [20]. For pure states, the bipartite entanglement between the subsystem i and the remaining combined system (jk) can be quantified by $\mathcal{T}_{i(jk)} = 2[1 - \text{Tr}(\rho_i^2)]$, where ρ_i is the reduced density matrix obtained from partially tracing over the systems j, k [21]. The different bipartite entanglements are not independent quantities, but must satisfy the Coffman-Kundu-Wootters (CKW) relation [22]

$$\mathcal{T}_{i(jk)}(|\psi\rangle) - \mathcal{T}_{ij}(|\psi\rangle) - \mathcal{T}_{ik}(|\psi\rangle) = \tau_{ijk}(|\psi\rangle), \quad (7)$$

where $|\psi\rangle$ is any three-qubit state and the *three-tangle* τ_{ijk} is the residual quantity that identifies tripartite entanglement. That is, $\tau_{ijk} \neq 0$ implies that the state cannot be written as a product of two states for any possible bipartition of the system. However, the converse is not true, that is, $\tau_{ijk} = 0$ does not imply that the state is biseparable. This is easily seen by considering the W states, which have null three-tangle even though they are not biseparable in any bipartition. Thus, the three-tangle entanglement defined in Eq. (6) represents only the GHZ-type genuine entanglement [12]. Defined in this way, τ_{ijk} is invariant under permutations of the indices ijk for pure states.

Let us now turn to mixed states. In this case, $2[1 - \text{Tr}(\rho_i^2)]$ is no longer the correct expression for $\mathcal{T}_{i(jk)}$, but becomes only an upper bound for it [23]. To determine this kind of bipartite entanglement for mixed states, we need a convex roof optimization considering all the pure-state decompositions of $\rho = \sum_i p_i |\phi_i\rangle\langle\phi_i|$, given by

$$\mathcal{T}_{i(jk)}(\rho) = \inf_{\{p_i, |\phi_i\rangle\}} \sum_i p_i \mathcal{T}_{i(jk)}(|\phi_i\rangle), \quad (8)$$

which is computationally expensive [24].

The residual multipartite entanglement for mixed states could be defined in analogy with the CKW relation Eq. (7). However, $\tau_{ijk}(\rho)$ is no longer invariant under permutations. Thus, for the case of mixed states, it is convenient to use the average over all the permutations of the indices $\{ijk\}$,

$$\tilde{\tau}_{ABE}(\rho) = \frac{1}{6} \sum_{\{ijk\}} \tau_{ijk}(\rho), \quad (9)$$

as the measure of tripartite entanglement.

As we mentioned above, a convex roof optimization is not a viable method for calculating $\mathcal{T}_{i(jk)}(\rho)$, but fortunately there are very good approximations for the case of quasipure (qp) states and lower bounds (LB) that capture the behavior of entanglement. Here we use the LB (see Ref. [25]) $\mathcal{T}_{i(jk)}^{\text{LB}} = 2(\text{Tr}[\rho^2] - \text{Tr}[\rho_i^2])$, where $\text{Tr}[\rho^2]$ is the purity of the total system. Substituting this LB into Eq. (7) gives a LB for the three-tangle, $\tau_{i(jk)}^{\text{LB}}$, where $\text{Tr}[\rho^2]$ is the purity of the total system.

The fact that quasipure states ρ_{qp} present a predominant eigenvalue in the spectral decomposition $\rho_{\text{qp}} = \sum_i \mu_i |\phi_i\rangle\langle\phi_i|$ such that $\mu_1 \gg \mu_i$ for $i > 1$, offers the possibility to obtain a good approximation for the concurrence $C_{i(jk)}$, as noted in Ref. [26]. This approximation is given by $C_{i(jk)}^{\text{qp}} = \max(0, s_1 - \sum_{i>1} s_i)$, where the s_i 's are the positive eigenvalues of a matrix $\tau^\dagger \tau$ defined in terms of the eigenvectors and eigenvalues of the matrix ρ_{qp} , as described in Ref. [26]. Defining $\mathcal{T}_{i(jk)}^{\text{qp}} = [C_{i(jk)}^{\text{qp}}]^2$, and substituting into Eq. (7) gives the three-tangle for the quasipure state.

Gathering the above results leads us to the following expressions for the LB and the quasipure approximation for the three-tangle:

$$\tau_{ijk}^{\text{LB/qp}}(\rho) = \mathcal{T}_{i(jk)}^{\text{LB/qp}}(\rho) - \mathcal{T}_{ij}(\rho) - \mathcal{T}_{ik}(\rho). \quad (10)$$

These expressions are also not invariant under permutations, so the average in Eq. (9) must be taken in order to define $\tilde{\tau}_{ABE}^{\text{LB}}(\rho)$, $\tilde{\tau}_{ABE}^{\text{qp}}(\rho)$.

We now use these expressions to analyze our experimental results. The overall purity of the initial ($p = 0$) target state (including systems A and B and the environment E), calculated from the reconstructed density matrix, was 0.92 ± 0.01 for the PD channel and 0.89 ± 0.01 for the AD channel. The lack of purity is due to technical problems [27]. We calculated the largest eigenvalue (μ_1) of all the density matrices for every values of p . All the values were greater than 0.85, and the mean value $\bar{\mu}_1 = 0.9$. This justifies the use of the quasipure approximation for τ_{ABE} . Figures 2(a) and 2(b) show the experimental results for the PD channel. Figure 2(a) shows the different tangles \mathcal{T}_{ij} obtained as a function of p . In all plots, the error bars are obtained from Monte Carlo simulations, assuming Poissonian photon counting statistics. The solid lines are the fittings, showing that the initial bipartite entanglement between the systems A and B disappears linearly. No bipartite entanglement is produced between any system and the environment during the evolution. In Fig. 2(b) we show the LB (blue squares) and quasipure (red circles) three-tangle entanglements as a function of p , as defined in Eq. (10). As soon as the interaction with the

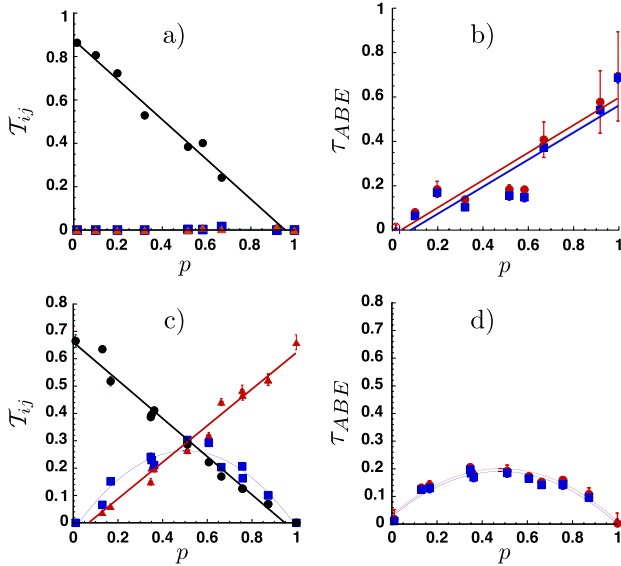


FIG. 2 (color online). Experimental results for the dynamics of entanglement. In (a), the dynamics of qubit-qubit entanglement for subsystems $A-B$ (black circles), $A-E$ (blue squares), and $B-E$ (red triangles) for the PD dynamics described by Eq. (4). In (b), we show the mean lower bound (blue squares) and mean quasi-pure approximation for the three-tangle entanglement (red circles). A linearly increasing behavior of the three-tangle case for both lower-bound (blue squares) and quasi-pure (red circles) approximation is observed. In (c), the dynamics of qubit-qubit entanglement, this time for AD interaction, for qubits $A-B$ (black circles), $A-E$ (red triangles), and $B-E$ (blue squares). A nonzero lower-bound (blue squares) and quasi-pure (red circles) approximation for the three-tangle case are displayed in (d).

environment is switched on, there is a nonzero LB to τ_{ABE} , witnessing the emergence of genuine multipartite entanglement. The increment in τ_{ABE} compensates the loss of bipartite entanglement. At $p = 1$, the tripartite entanglement τ_{ABE} reaches its maximum value and all the qubit-qubit entanglements vanish. At this point, the tripartite system is in a GHZ state.

The experimental results for the AD channel are shown in Figs. 2(c) and 2(d). The tangle between the different pairs of qubits shown in Fig. 2(c) illustrates not only the disappearance of the initial entanglement between the qubits A and B but also the increasing entanglement in $A-E$ and $B-E$. The three bipartite tangles reach almost the same value for $p = 0.5$, where, from Eq. (6), the whole system is in a W state. Figure 2(d) shows the three-tangle LB (blue squares) and quasipure (red circles) approximations for this evolution. We observe non-negligible amounts of three-tangle entanglement, with a maximum near $p = 0.5$, even though the three-tangle entanglement for a pure W state should be exactly zero. This genuine entanglement, as measured by τ_{ABE} , is thus a consequence of the impurity of the state. We can verify this by analyzing the spectrum of the measured density matrix ρ for $p = 0.5$. The spectrum shows that the maximum eigenvalue μ_1 is

0.95, and the corresponding eigenvector $|\phi_1\rangle$ has a fidelity with respect to the W state of $F_W(|\phi_1\rangle) = 0.98 \pm 0.01$. The same $|\phi_1\rangle$ presents $\tau_{ABE} = 0$, which implies that the contributions to the nonzero three-tangle entanglement come from the other components of the state. It is interesting to observe that even though the additional contributions to the spectral decomposition of ρ are small, in view of the high purity ($= 0.90 \pm 0.01$) of ρ for $p = 0.5$, their global effect is considerable, resulting in a three-tangle entanglement that is nearly one-third of the initial bipartite entanglement. This shows that τ_{ABE} is very sensitive to the mixedness of a state.

In order to better capture the emergence of genuine tripartite entanglements, we calculate two alternative indicators of genuine entanglements for all values of p : (i) a recently derived criteria for genuine entanglement in the form of inequalities [28], and (ii) the fidelities with respect to GHZ and W states, which witness entanglements for their respective classes. Genuine entanglements can be confirmed for $F_{\text{GHZ}} \geq 1/2$ or $F_W \geq 2/3$ [29].

To detect genuine entanglements, one of the following inequalities in terms of the matrix elements of the tripartite state must be violated [28]:

$$K_{\text{GHZ}} = |\rho_{18}| - \sqrt{\rho_{22}\rho_{77}} - \sqrt{\rho_{33}\rho_{66}} - \sqrt{\rho_{44}\rho_{55}} \leq 0, \quad (11)$$

$$K_W = |\rho_{23}| + |\rho_{25}| + |\rho_{35}| - \sqrt{\rho_{11}\rho_{44}} - \sqrt{\rho_{11}\rho_{66}} - \sqrt{\rho_{11}\rho_{77}} - 1/2(\rho_{22} + \rho_{33} + \rho_{55}) \leq 0. \quad (12)$$

The entanglement that these criteria detect is not defined as a residual quantity, as in Eq. (7). They detect the non-biseparability of the state for any bipartition and capture the genuine entanglement contained in the W states, which is not taken into account by τ_{ABE} .

Figure 3 shows the behavior of these quantities for the two scenarios discussed above. For the PD evolution, Fig. 3(a) shows that as p increases, the tripartite state becomes very close to the GHZ state, with maximum fidelity at the end of the evolution ($p = 1$). F_{GHZ} already detects genuine entanglements from the third point on (corresponding to $p = 0.19 \pm 0.01$), while the criterion (11) shown in Fig. 3(b) detects genuine entanglements for any value of p different from 0.

For the AD evolution, Fig. 3(c) displays the fidelity F_W , which reaches its maximum value for $p = 0.5$. The criteria Eq. (12) reveals considerable experimental violations for any value of p different from 1 or 0, serving as an excellent indicator of nonbiseparability.

Our interferometric setup allows for the implementation of quantum channels through the coupling of polarization degrees (qubits) with spatial modes that act as environments. We show that for PD, the initial bipartite entanglement gets completely transformed into a genuine GHZ-like entanglement. The inclusion of the environment in our investigation helps us understand the peculiar asymptotic

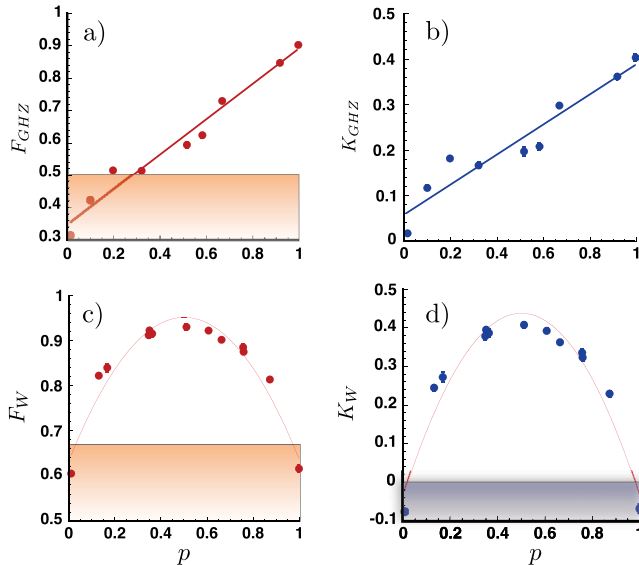


FIG. 3 (color online). Experimental results for the dynamics of indicators of genuine entanglement: (a) Fidelity with respect to GHZ state and PD channel. (b) Criterion for genuine entanglement detection of Ref. [28] for the PD channel. (c) Fidelity with respect to the W state, AD channel (d) Criterion for genuine entanglement for AD channel.

situation, where the initial bipartite entanglement vanishes for any two subsystems. For the amplitude damping channel, the initial bipartite entanglement leads to a transient appearance of W -like states. This could be the first step in a more thorough investigation of the imprint of an initial multipartite entanglement onto more complex environments.

Financial support was provided by Brazilian agencies CNPq, CAPES, FAPERJ, and the Instituto Nacional de Ciência e Tecnologia-Informação Quântica. A.V.H was funded by the Consejo Nacional de Ciencia y Tecnología, México.

[1] D. Giulini, E. Joos, C. Kiefer, J. Kupsch, I.-O. Stamatescu, and H. Zeh, *Decoherence and the Appearance of a Classical World in Quantum Theory* (Springer-Verlag, Berlin, 1987).
 [2] W. H. Zurek, *Rev. Mod. Phys.* **75**, 715 (2003).
 [3] M. Cornelio, F.F. Fanchini, I. Frérot, G.H. Aguilar, M.O. Hor-Meyll, M.C. de Oliveira, S.P. Walborn, A.O. Caldeira, and P.H.S. Ribeiro, [arXiv:1203.5068](https://arxiv.org/abs/1203.5068).
 [4] T. Yu and J.H. Eberly, *Phys. Rev. Lett.* **93**, 140404 (2004).
 [5] M.P. Almeida, F. de Melo, M. Hor-Meyll, A. Salles, S.P. Walborn, P.H.S. Ribeiro, and L. Davidovich, *Science* **316**, 579 (2007).
 [6] L. Aolita, R. Chaves, D. Cavalcanti, A. Acín, and L. Davidovich, *Phys. Rev. Lett.* **100**, 080501 (2008).
 [7] C.E. Lopez, G. Romero, F. Lastra, E. Solano, and J.C. Retamal, *Phys. Rev. Lett.* **101**, 080503 (2008).

[8] A. Salles, F. de Melo, M.P. Almeida, M. Hor-Meyll, S.P. Walborn, P.H. Souto Ribeiro, and L. Davidovich, *Phys. Rev. A* **78**, 022322 (2008).
 [9] R. Blume-Kohout and W.H. Zurek, *Phys. Rev. A* **73**, 062310 (2006).
 [10] W.H. Zurek, *Nature Phys.* **5**, 181 (2009).
 [11] O. Jiménez Farías, A. Valdés-Hernández, G.H. Aguilar, P.H. Souto Ribeiro, S.P. Walborn, L. Davidovich, X.-F. Qian, and J.H. Eberly, *Phys. Rev. A* **85**, 012314 (2012).
 [12] W. Dür, G. Vidal, and J.I. Cirac, *Phys. Rev. A* **62**, 062314 (2000).
 [13] D. Greenberger, M. Horne, and A. Zeilinger, *Bell's Theorem, Quantum Theory and Conceptions of the Universe* (Kluwer, Dordrecht, 1989).
 [14] P.G. Kwiat, E. Waks, A.G. White, I. Appelbaum, and P.H. Eberhard, *Phys. Rev. A* **60**, R773 (1999).
 [15] D.N. Biggerstaff, R. Kaltenbaek, D.R. Hamel, G. Weihs, T. Rudolph, and K.J. Resch, *Phys. Rev. Lett.* **103**, 240504 (2009).
 [16] K.A.G. Fisher, R. Prevedel, R. Kaltenbaek, and K.J. Resch, *New J. Phys.* **14**, 033016 (2012).
 [17] This is accomplished by positioning a BD between two HWP's at $\frac{\pi}{4}$.
 [18] M. Nielsen and I. Chuang, *Quantum Computation and Quantum Information* (Cambridge University, Cambridge, England, 2000).
 [19] O. Jiménez Farías, C.L. Latune, S.P. Walborn, L. Davidovich, and P.H.S. Ribeiro, *Science* **324**, 1414 (2009).
 [20] W.K. Wootters, *Phys. Rev. Lett.* **80**, 2245 (1998).
 [21] P. Rungta, V. Buzek, C.M. Caves, M. Hillery, and G.J. Milburn, *Phys. Rev. A* **64**, 042315 (2001).
 [22] V. Coffman, J. Kundu, and W.K. Wootters, *Phys. Rev. A* **61**, 052306 (2000).
 [23] Z.G. Li, S.M. Fei, S. Albeverio, and W.M. Liu, *Phys. Rev. A* **80**, 034301 (2009).
 [24] R. Horodecki, P. Horodecki, M. Horodecki, and K. Horodecki, *Rev. Mod. Phys.* **81**, 865 (2009).
 [25] F. Mintert and A. Buchleitner, *Phys. Rev. Lett.* **98**, 140505 (2007).
 [26] F. Mintert and A. Buchleitner, *Phys. Rev. A* **72**, 012336 (2005).
 [27] These include the broadness of the interference filters used in the SPDC source, the eventual misalignment of the two interferometers, the mismatch between light beams coming from different paths, the statistical fluctuations of the incoming photons and the refraction index of the air, and also the low overall visibility, in spite of the high visibility of each interferometer (approximately 0.95). This is due to the fact that three interference processes—one for each pair of beam displacers in Fig. 1—are involved in the preparation and measurement of the tripartite state ABE , leading to an effective visibility approximately equal to $(0.95)^3 \approx 0.86$.
 [28] O. Gühne and M. Seevinck, *New J. Phys.* **12**, 053002 (2010).
 [29] A. Acín, D. Bruß, M. Lewenstein, and A. Sanpera, *Phys. Rev. Lett.* **87**, 040401 (2001).